XL-SIM: extending superresolution into deeper layers

Martin Schropp, Christian Seebacher, Rainer Uhl

Supplementary figures and text:

Supplementary Figure 1: 3D model of the microscope platform

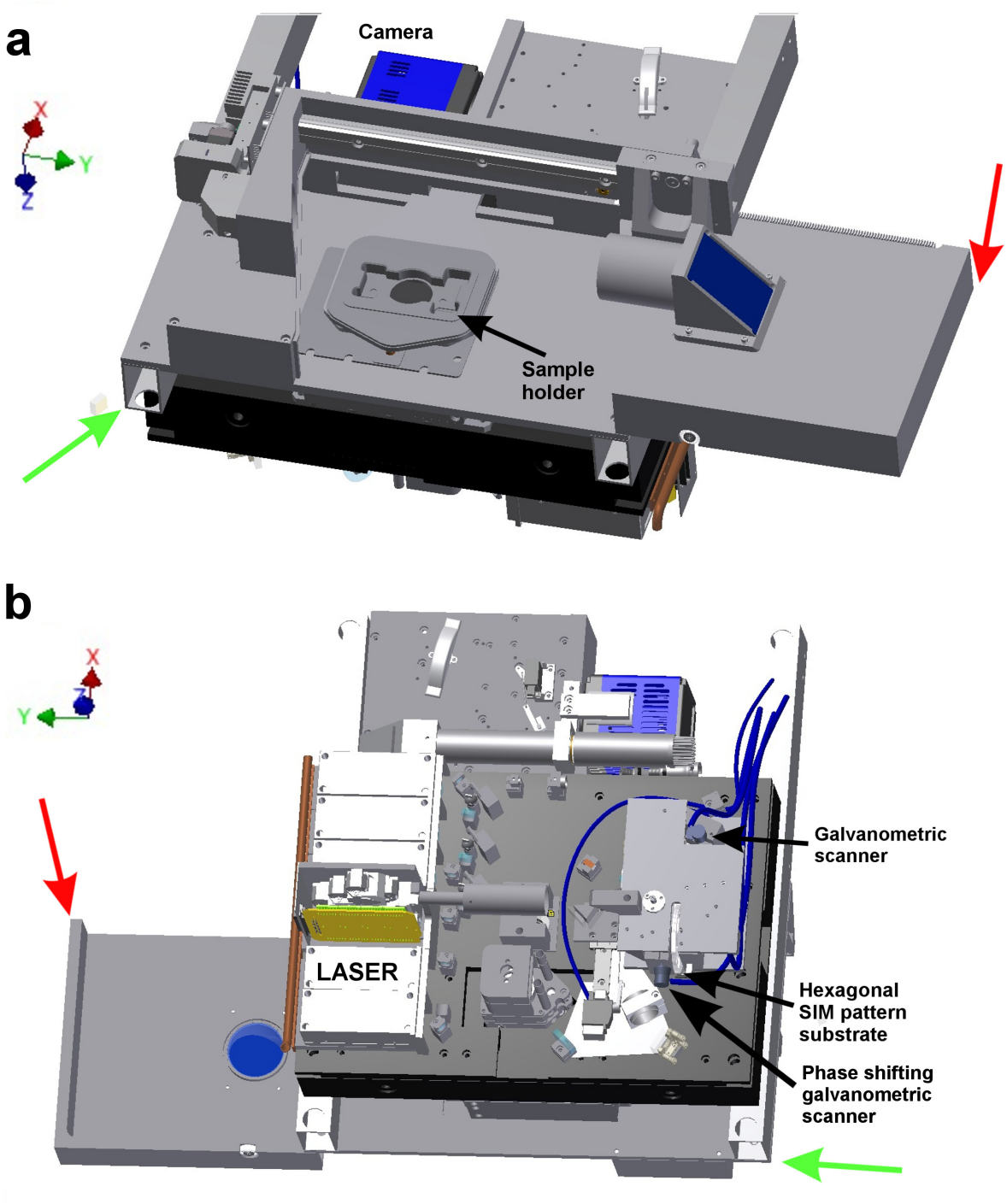

Figure S1: (a) Top view of the used microscope platform. (b) Bottom view. Note that device edges marked by the green and red arrows correspond in (a) and (b). The excitation beam path as schamatically illustrated in supplementary figure X can be seen in (b).

Supplementary Figure 2: Comparison of line shaped and epifluorescent hexagonal SIM excitation

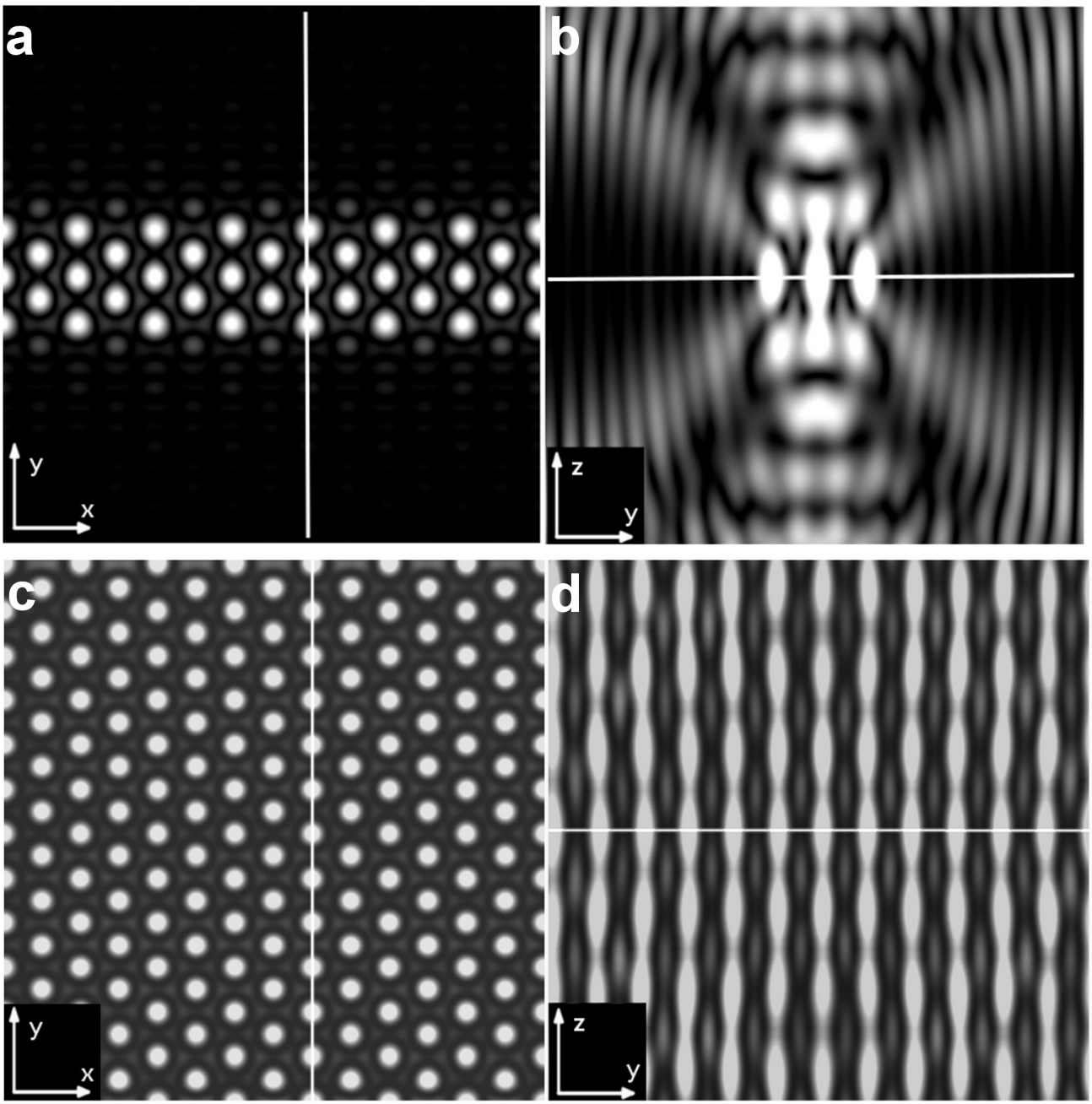

Figure S2: a) and b) correspond to figure 1b). The hexagonal intensity for an epifluorescent (non confocal) excitation is shown in c) and d). All the Talbot layers in c) and d) have the same contrast. The locations of intensity maxima in (x, y) coincide for all layers. In contrast to that, one sees the symmetry break in b), which shifts the intensity maxima towards the center of the line (for the drawn point in time/excitation line location). A variation of the positions of the hexagonal intensity maxima relative to the line position (which is given, if the line is scanned across the sample) thus leads to a variation of the location of the intensity maxima relative to the sample coordinate frame in the non focus Talbot layers. This effect is illustrated in supplementary video 1.

Supplementary Figure 3: Geometry of hexagonal frequency vectors in the case of plane illumination

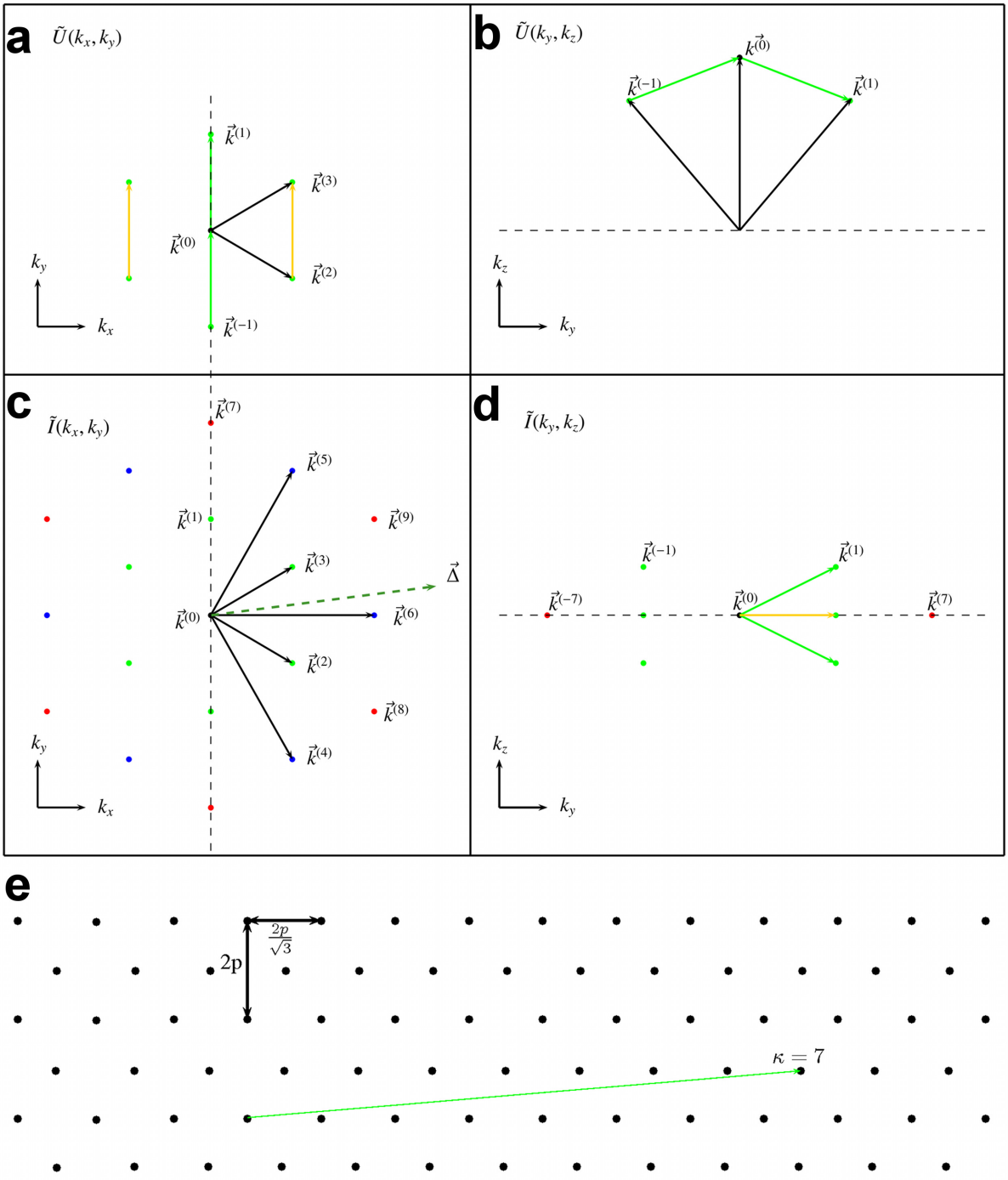

Figure S3: (a) (x/y) view of the hexagonal amplitude frequency vectors, which are also shown in figure 1a). The (y/z) view of the frequency vectors is shown in b). Corresponding intensity frequency vectors are shown in c) and d). The intensity frequency vector $\vec{k}^{(1)}$, which is also indicated in a) and b) is split into a pure lateral frequency (orthogonal to the k_z-direction, indicated in yellow) and a frequency which employs a k_z component also (indicated in green). The geometry of the hexagonal pattern in real space is shown in e). The used shift vector $\vec{\Delta}$ is indicated as a green arrow.

Supplementary Figure 4: Theoretical integrated excitation contrasts as a function of the excitation line widths

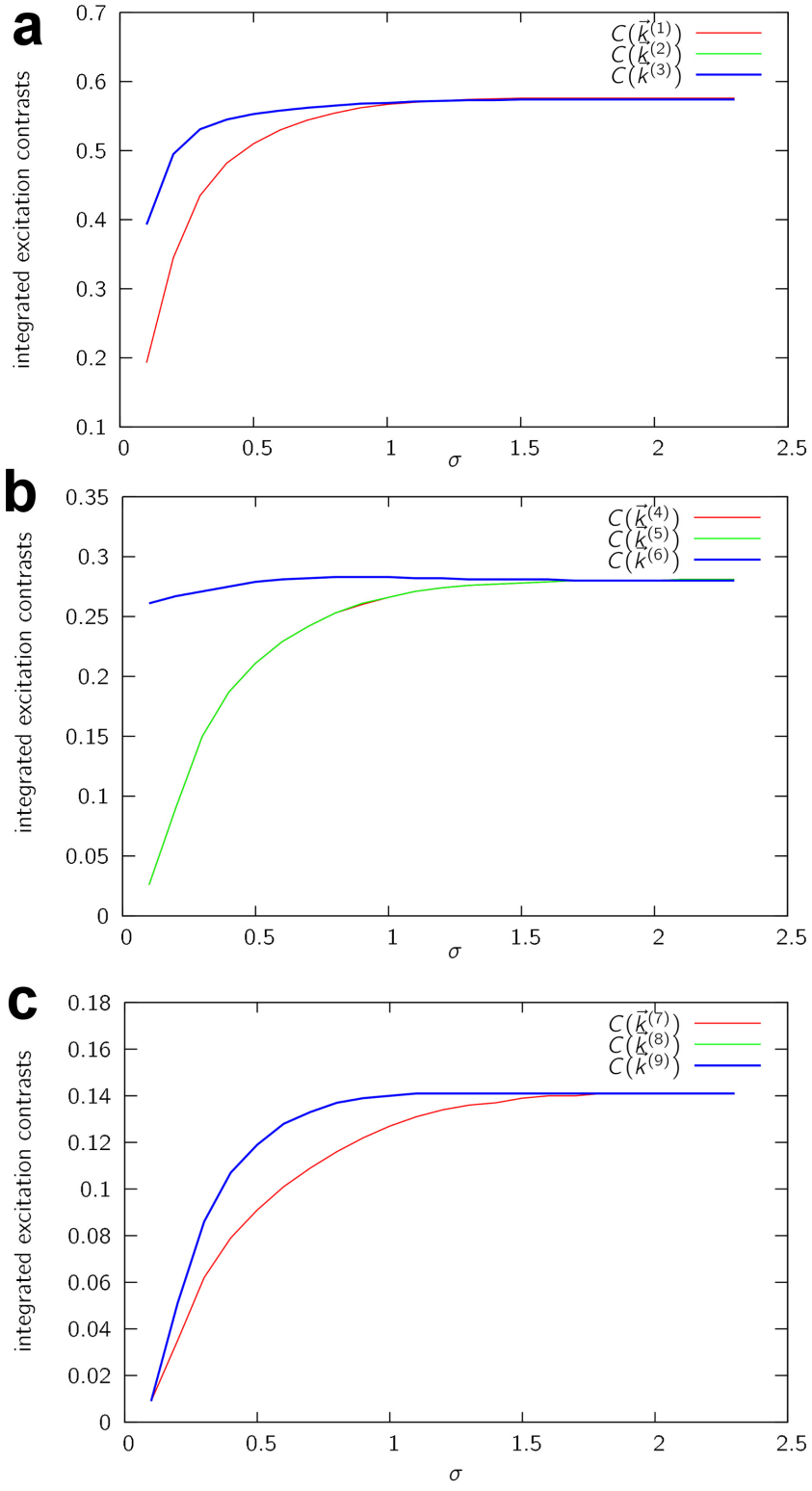

Figure S4: The excitation lines were assumed to have a Gaussian profile with a root mean square of σ, where σ is measured in units of hexagon periods p. Choosing a line width of $\sigma \approx 1.6p$ bigger gives an homogeneous distribution of integrated excitation contrasts.

Supplementary Figure 5: Drawing of the hexagonal phase pattern design

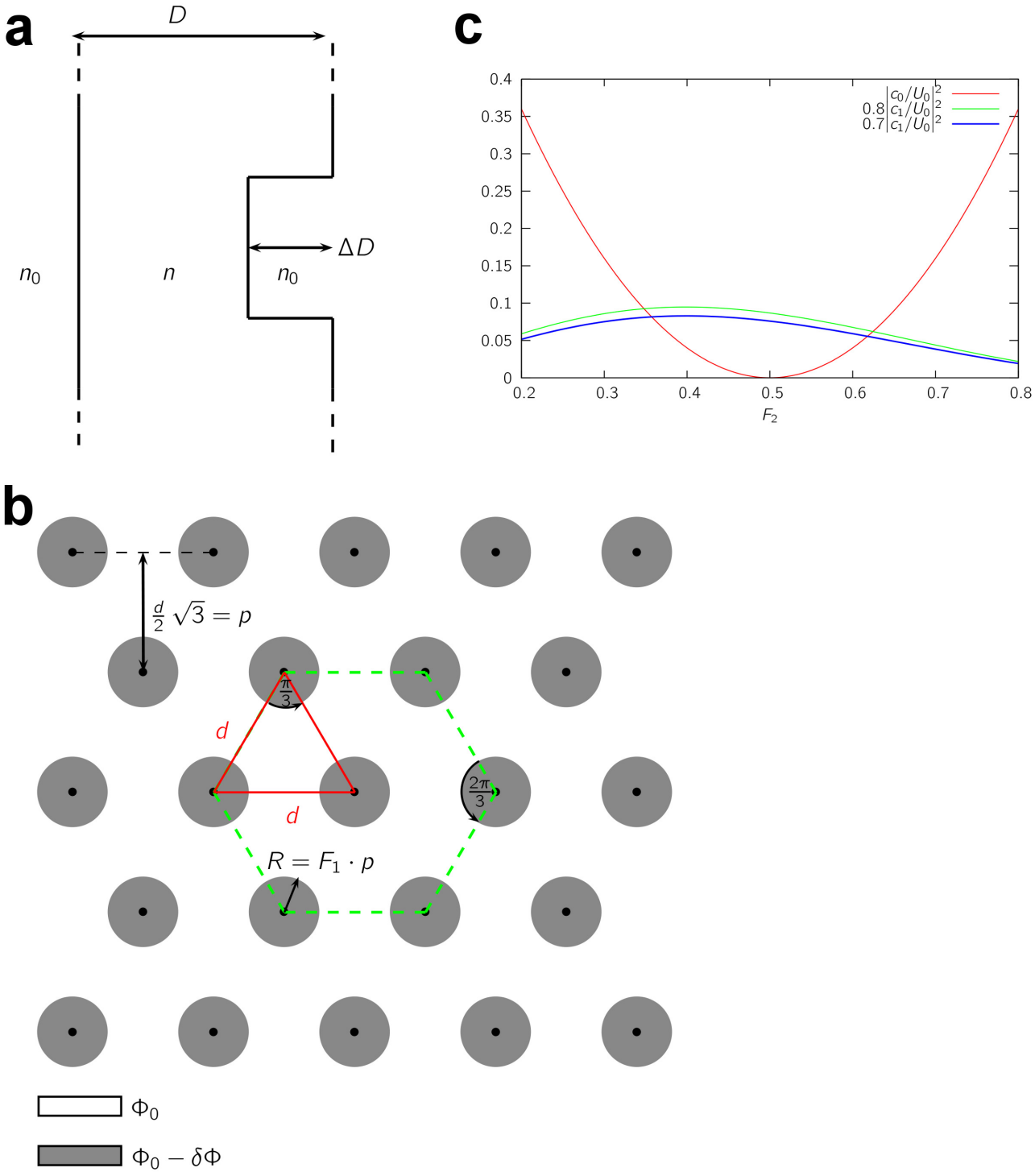

Figure S5: a) As in [S1] a phase pattern has been used for SIM. The pattern is modulated in the optical path differences of light transmitting through the substrate. b) Geometry of hexagonal path/phase differences. Light passing the grayed areas of the substrate are phase shifted by a phase difference of $\delta\Phi$. The fill-factor F_1 is the ratio of the circle radius and the pattern period and is chosen analogously to [S1], which means that the zero hexagonal diffraction order has approximately 70 – 80% of the first diffraction order's power in the pupil of the objective. This leads to totally 7 diffraction orders with approximately the same power in the sample.

Supplementary Figure 6: Fourier coefficients of the hexagonal illumination intensity in table 2 as functions of the linear polarization angle χ

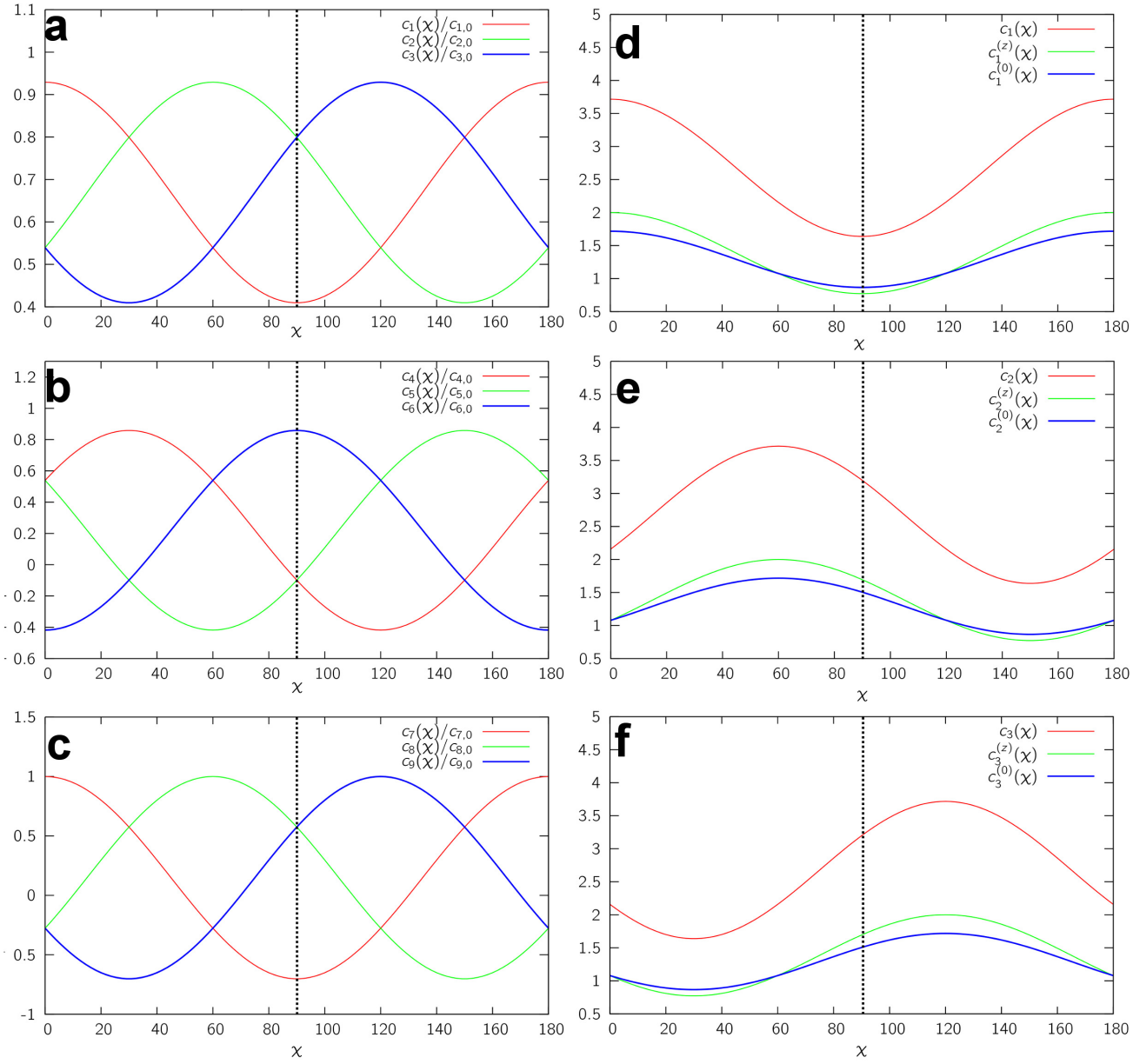

Figure S6: The diffraction angle α was assumed to be $\alpha \approx 67.3°$. (a)-(c) Fourier coefficients for the hexagonal frequencies $\vec{k}^{(1)}$ - $\vec{k}^{(9)}$. The coefficients are normed to their respective values without the influence of polarization ($c_{n,0}$). In our experiments, we chose a linear polarization direction of $\chi = 90°$ orthogonal to the excitation line.

The Fourier coefficients for the base frequencies $\vec{k}^{(1)}$, $\vec{k}^{(2)}$ and $\vec{k}^{(3)}$ can be split into a z-independent contribution ($c_n^{(0)}$) and a contribution that depends on the defocus z ($c_n^{(z)}$). The corresponding coefficients which are summarized in table 3 are plotted in (d), (e) and (f).

Supplementary Figure 7: Simulation of the frequency vectors errors on the resolution and homogeneity of Superresolution SIM

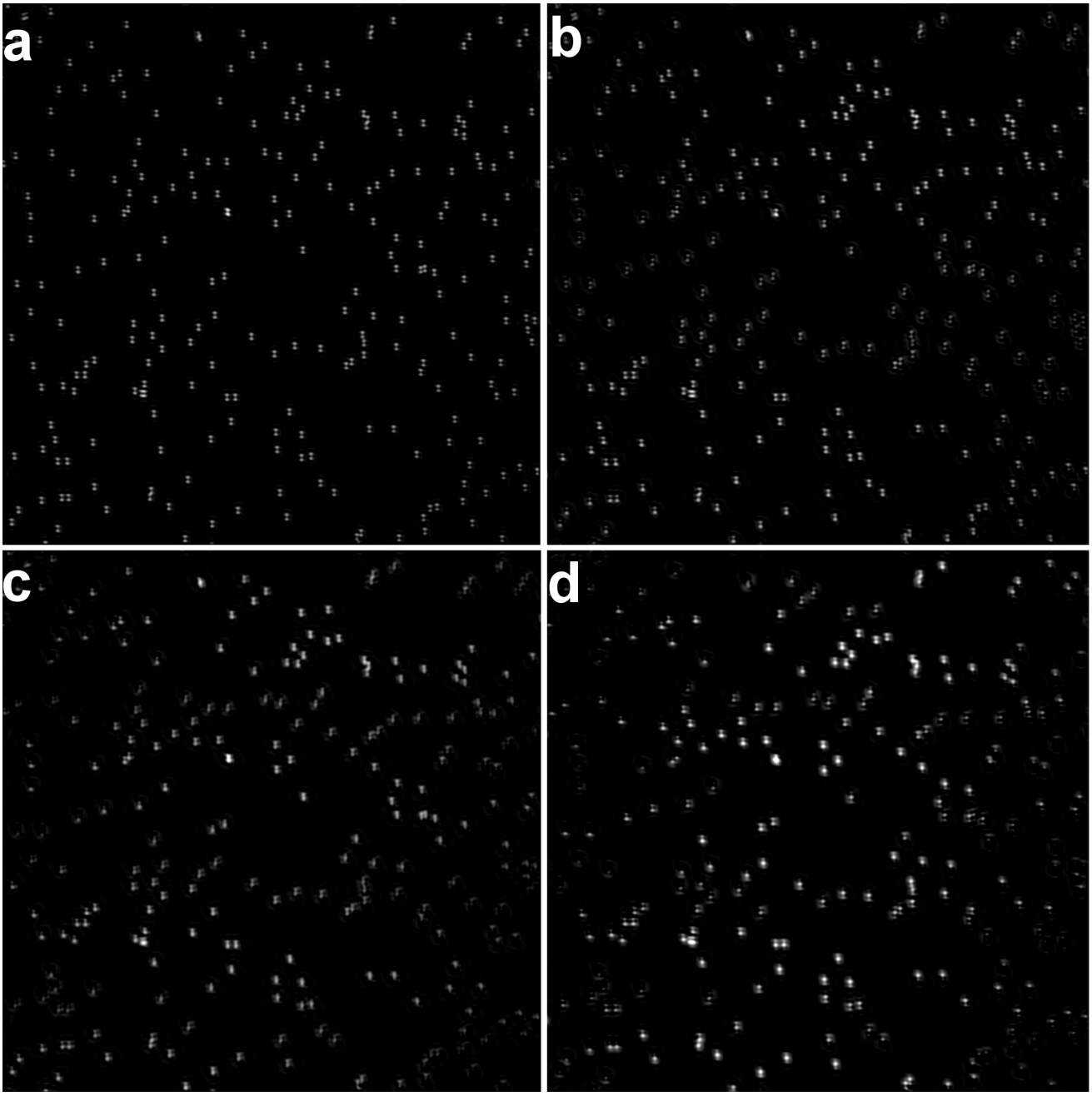

Figure S7: 300 Nanorulers with a distance of 120nm (all orientated in y-direction) were assumed as object. The absolute values of the frequencies have been assumed to be known and without errors, thus the only error source is the orientation of the frequency vectors. a) SIM image without frequency errors. b) An error of 5mrad has been assumed. c) and d) show the SIM image for an error of 1% and 1.5% respectively.

Supplementary Figure 8: Full field of view for the measurement in figure 4d) and 4e)

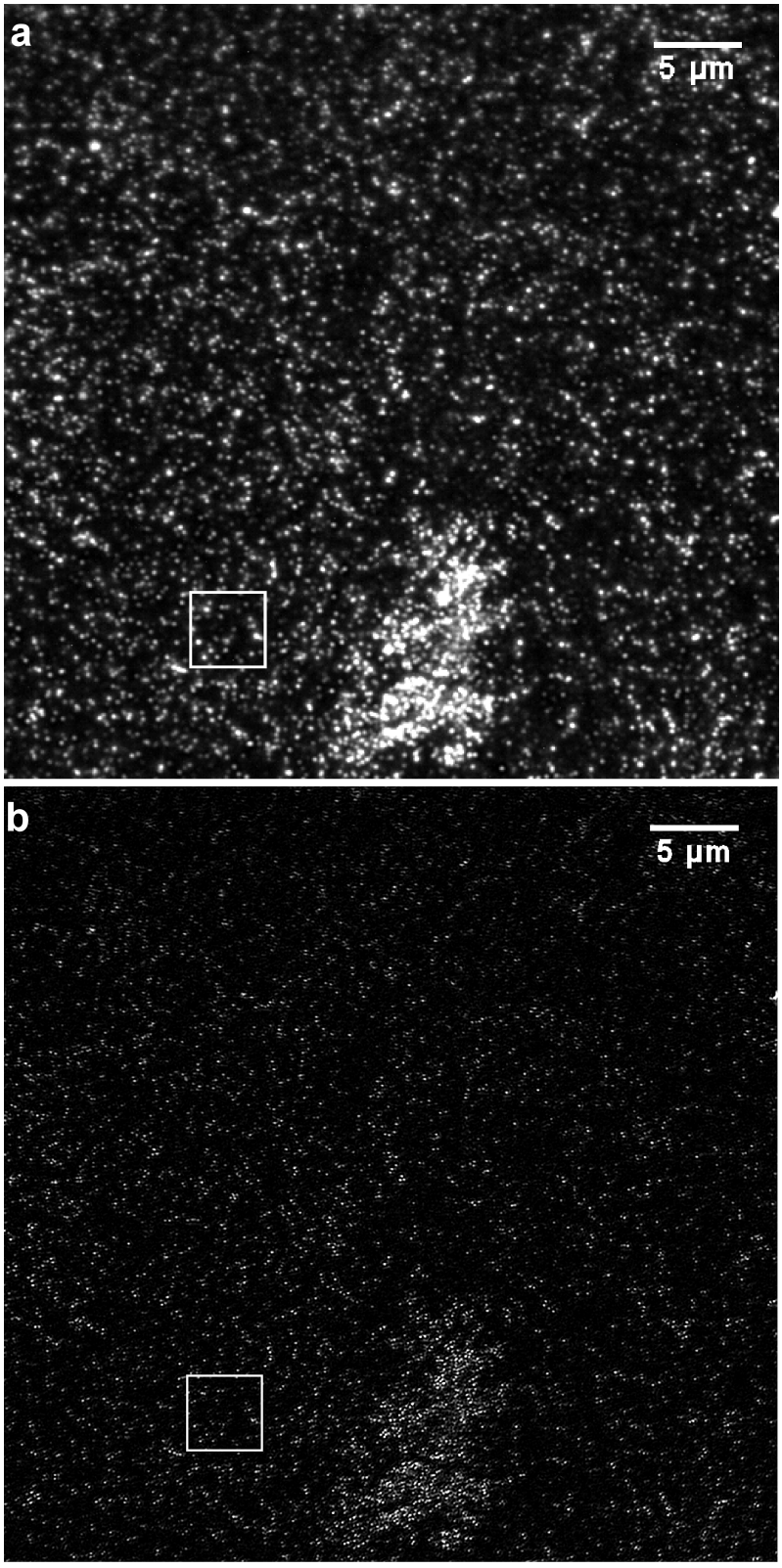

Figure S8: a) shows a line-confocal image and b) an XL-SIM image. The ROI shown in figure 3d) and 3e) is indicated as a white box.

Supplementary Figure 9: Line-confocal PSF – Averaged PSF from figure S8a)

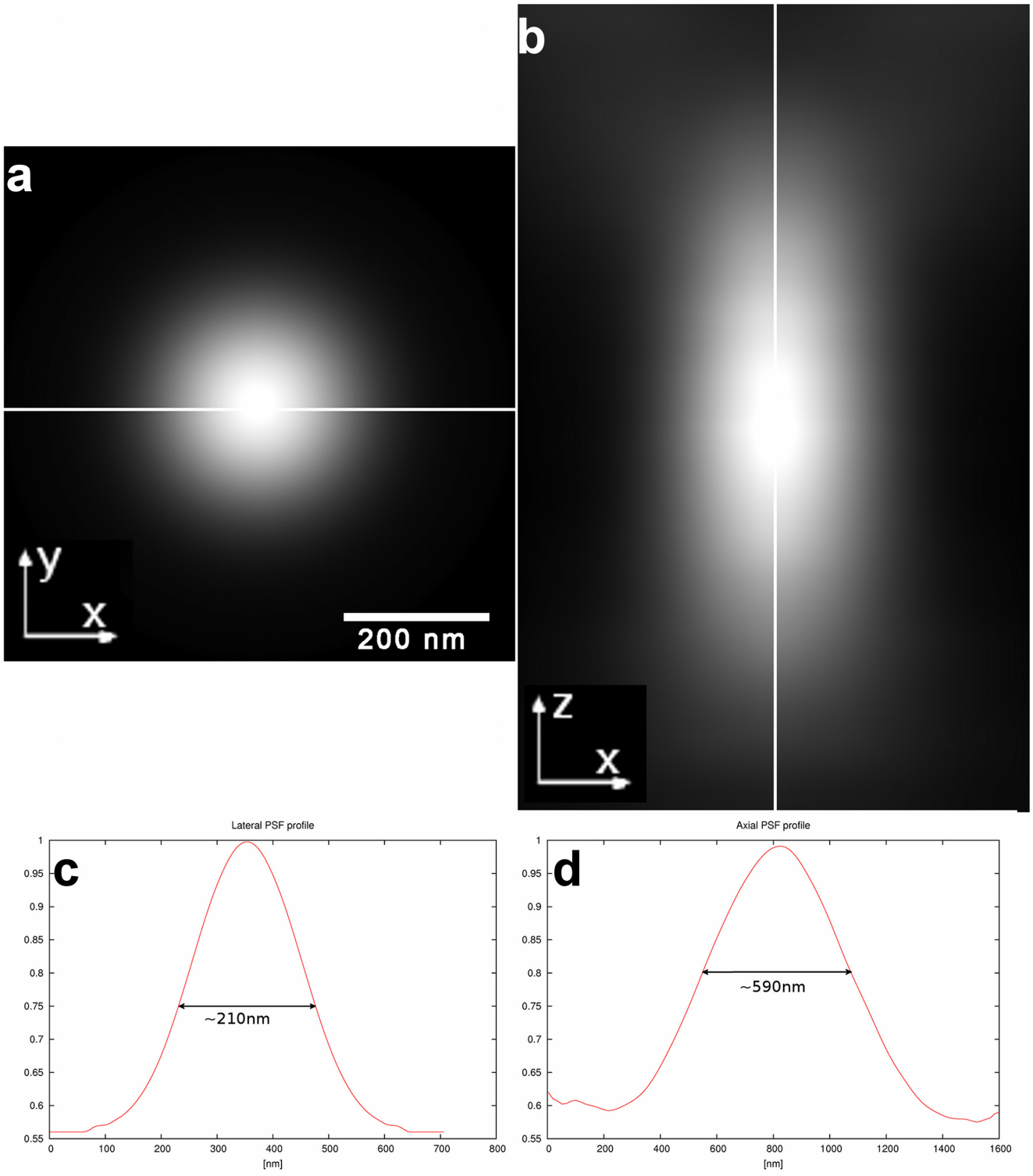

Figure S9: 10 intensity profiles from the measurement in figure 3d) and 3g) have been superimposed with subpixel accuracy and radially averaged. The resulting (x/y) and (x/z) PSF intensity sections are shown in (a) and (b). Pixel sizes in (x/y) equal pixel sizes in (x/z). The intensity profiles along the white lines in () and b) are plotted in c) and d).

Supplementary Figure 10: XL-SIM PSF – Averaged PSF from figure S8B)

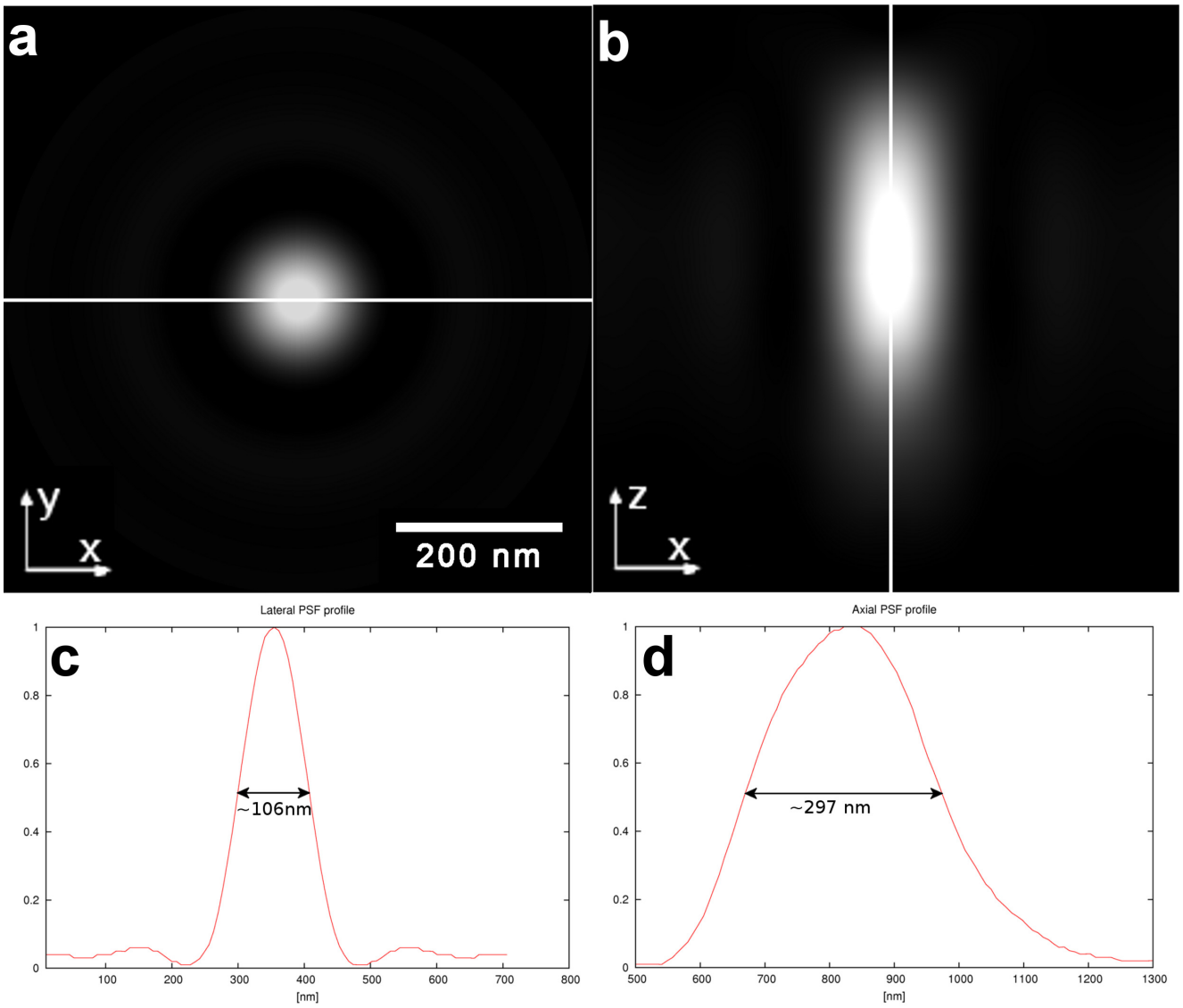

Figure S10: 10 isolated bead volumes from the measurement in figure 3e) (or figure S8) have been superimposed with subpixel accuracy and radially averaged. The resulting (x/y) and (x/z) PSF intensity sections are shown in a) and b). The intensity profiles along the white lines in a) and b) are plotted in c) and d).

Supplementary Figure 11: Line-confocal SIM pattern contrast on a *Chroma* slide

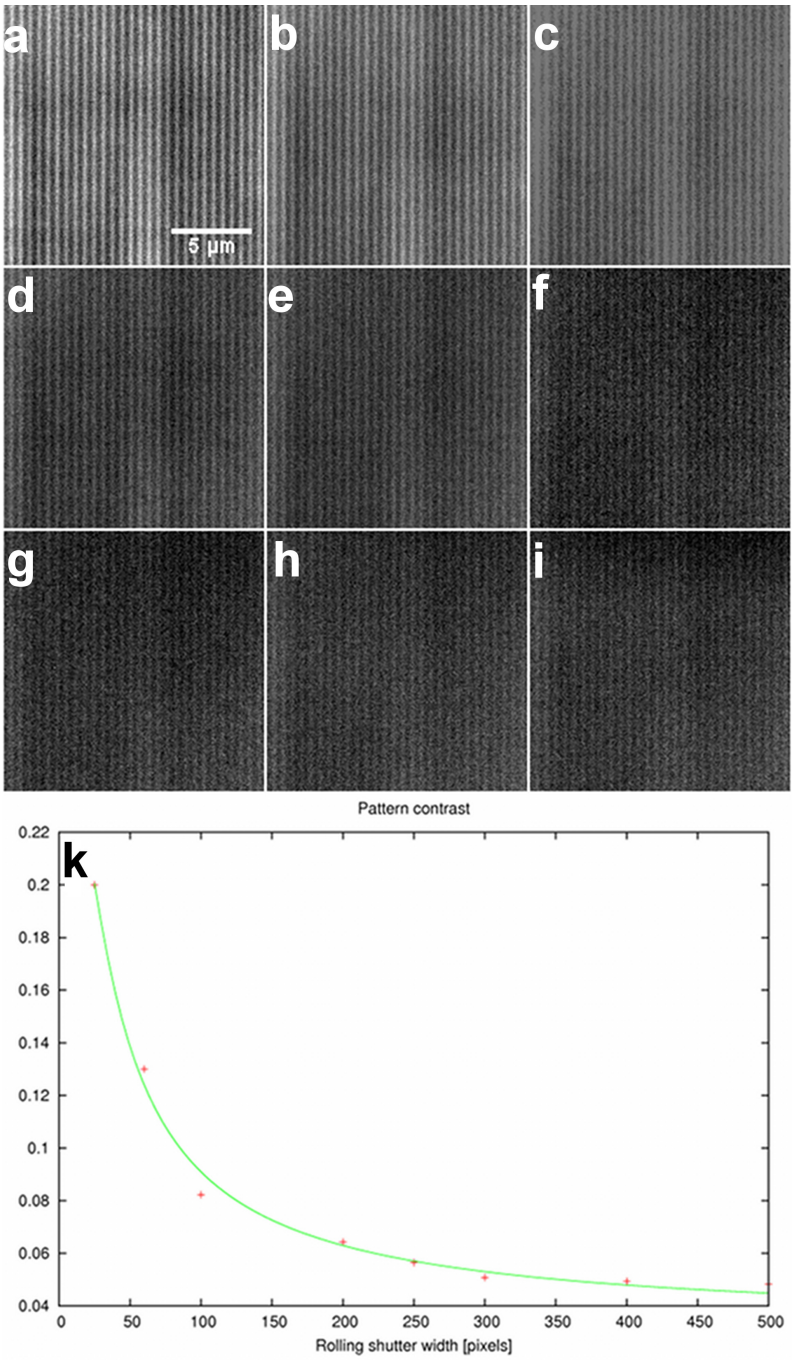

Figure S11: Illustration of out of focus suppression by the rolling shutter. An amplitude modulated line grid pattern substrate (as used for quasiconfocal SIM as e.g. in [S2]) was imaged onto an auto-fluorescent plastic slide from the company *Chroma*. a) - i) show SIM phase images for different rolling shutter widths: a) 25, b) 50, c) 100, d) 150, e) 200, f) 250, g) 300, h) 400 and i) 500 pixels. The rolling shutter widths are plotted versus the corresponding pattern contrasts in k).

Supplementary Figure 12: Two XL-SIM images from nanoruler sample

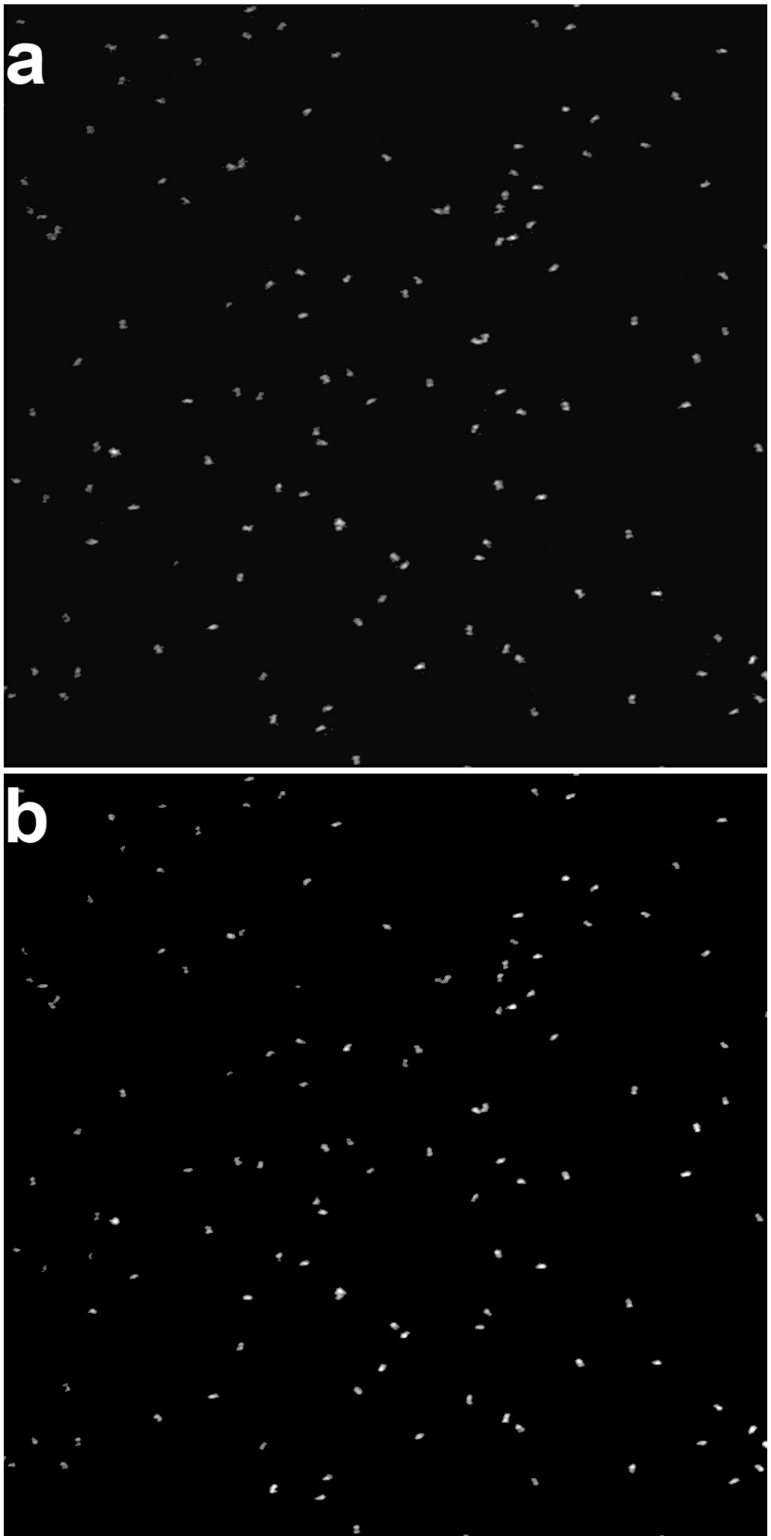

Figure S12: A set of 76 phase images was split in two sets of 38 phase images each and two statistically independents XL-SIM images have been processed. These two XL-SIM images are shown in a) and b) and have been used for the caldulation of the FRC (see figure 3a)-c)).

Supplementary Figure 13: Full fild of view for the measurement in figure 6a) and 6b)

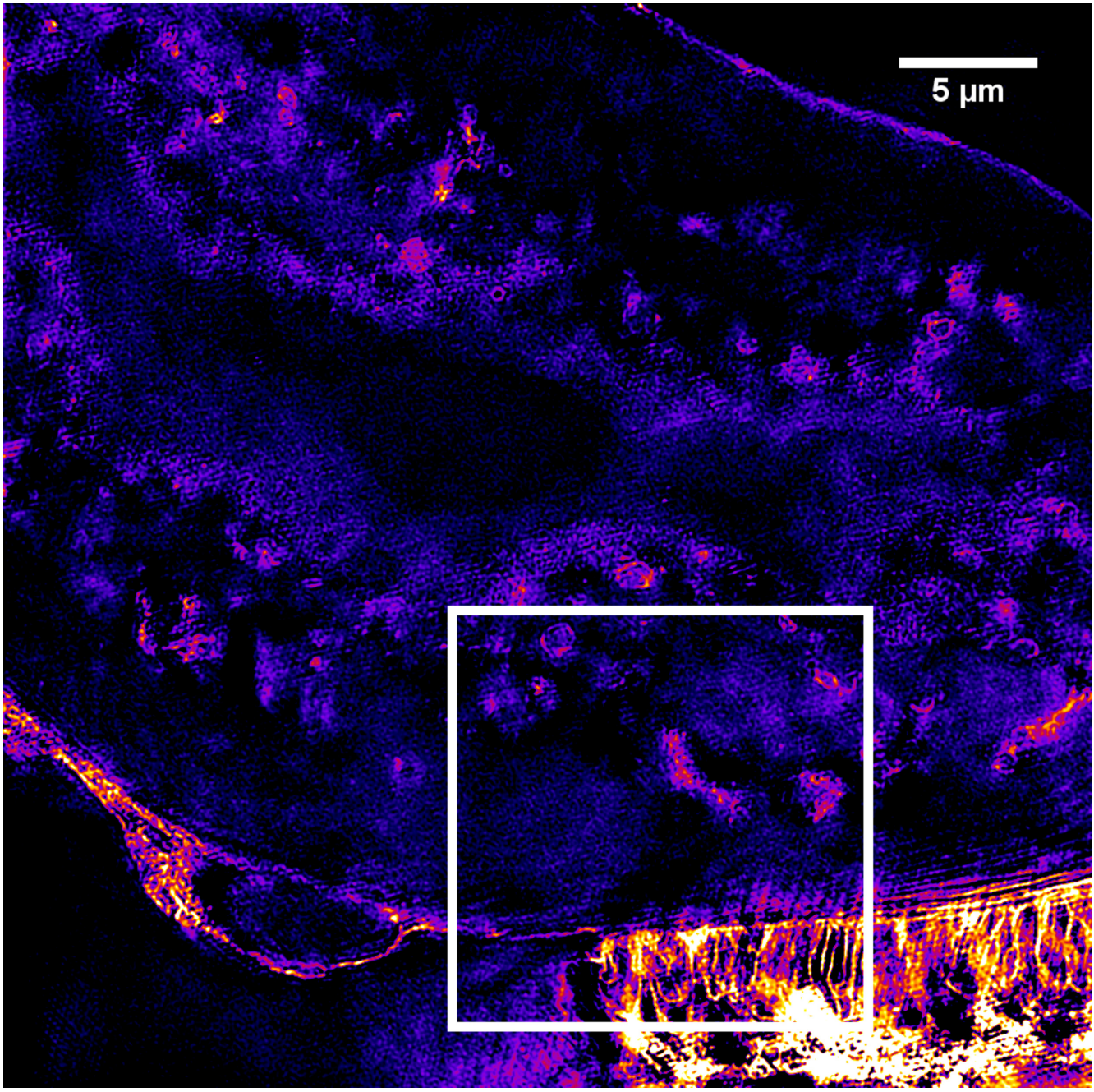

Figure S13: SIM measurement of line-grid SIM: The white box marks the ROI shown in figure 6a) and 6b).

Supplementary Note 1: Shift angles of the hexagonal pattern

This section shows the derivation of the correct shift angles for the hexagonal pattern. The line-shaped excitation is neglected in this section.

The main idea of using hexagonal (and also chequerboard) patterns for SIM with only one single shift direction has been described in [S3]. In contrast to [S3], we use an hexagonal phase pattern (as shown in figure S5), which is illuminated coherently by a line shaped partial coherent wave. Because the line shape of the illumination does not influence hexagonal frequency vectors and shift directions of the pattern intensity, it is neglected in the following.

The amplitude distribution of the hexagonal phase pattern is represented by dots in figure S3a). The period of the hexagonal phase pattern is chosen such, that there are in total 7 diffraction orders, which can pass the objective's pupil. In the chosen coordinate system, they are given by the 0.th diffraction order $\vec{k}^{(0)}$(draw in black),

$$\vec{k}^{(1)} = \frac{2\pi}{p}\begin{pmatrix}0\\1\end{pmatrix} \qquad \vec{k}^{(2)} = \frac{\pi}{p}\begin{pmatrix}\sqrt{3}\\-1\end{pmatrix} \qquad \vec{k}^{(3)} = \frac{\pi}{p}\begin{pmatrix}\sqrt{3}\\1\end{pmatrix}, \tag{S1}$$

and their negative counterparts $\vec{k}^{(-1)} = -\vec{k}^{(1)}$, $\vec{k}^{(-2)} = -\vec{k}^{(2)}$, $\vec{k}^{(-3)} = -\vec{k}^{(3)}$ (drawn as green dots). The section through the (k_x, k_y) plane is shown in figure S3b). Note, that the dashed line in figure S3b) corresponds to the dashed line in figure S3a). The spatial intensity spectrum $\tilde{I}(\vec{k}_x, k_y, k_z)$ is given by the autocorrelation of the amplitude spectrum $\tilde{U}(k_x, k_y, k_z)$. Thus all frequencies which are contained in the intensity spectrum are given by all possible difference frequencies of $\tilde{U}(k_x, k_y, k_z)$. The lateral intensity spectrum $\tilde{I}(k_x, k_y)$ is drawn in figure S3c). The difference vectors which give $\vec{k}^{(1)}$ in the intensity spectrum are drawn as green and yellow arrows in figure S3a) and S3b). There are two possible difference vectors, which have a k_z component (green) and two difference vectors in the (k_x, k_y) plane. Thus, the (intensity) frequency $\vec{k}^{(1)}$ in figure S3c) is split into three contributions along the k_z axis. Only the intensity frequencies $\vec{k}^{(1)}$, $\vec{k}^{(2)}$ and $\vec{k}^{(3)}$ have a non-zero k_z component. Thus, only these three frequencies have a contrast profile which is not constant relative to the z direction.

In total, the 7 frequencies contained in $\tilde{U}(\vec{k})$ lead to 31 frequencies in $\tilde{I}(\vec{k})$. Because a phase image only contains lateral frequency components, there are totally 19 frequency components contained in one phase image.

Those frequency vectors are $\vec{k}^{(0)} = \vec{0}$,

$$\vec{k}^{(1)} = \frac{2\pi}{p}\begin{pmatrix}0\\1\end{pmatrix}, \qquad \vec{k}^{(2)} = \frac{\pi}{p}\begin{pmatrix}\sqrt{3}\\-1\end{pmatrix}, \qquad \vec{k}^{(3)} = \frac{\pi}{p}\begin{pmatrix}\sqrt{3}\\1\end{pmatrix}, \tag{S2}$$

$$\vec{k}^{(4)} = \frac{\pi}{p}\sqrt{3}\begin{pmatrix}1\\-\sqrt{3}\end{pmatrix}, \qquad \vec{k}^{(5)} = \frac{\pi}{p}\sqrt{3}\begin{pmatrix}1\\\sqrt{3}\end{pmatrix}, \qquad \vec{k}^{(6)} = \frac{2\pi}{p}\sqrt{3}\begin{pmatrix}1\\0\end{pmatrix},$$

$$\vec{k}^{(7)} = \frac{2\pi}{p}\begin{pmatrix}0\\2\end{pmatrix}, \qquad \vec{k}^{(8)} = \frac{\pi}{p}\begin{pmatrix}2\sqrt{3}\\-2\end{pmatrix}, \qquad \vec{k}^{(9)} = \frac{\pi}{p}\begin{pmatrix}2\sqrt{3}\\2\end{pmatrix}$$

and their negative counterparts. The frequency vectors are connected by the following relations:

$$\vec{k}^{(3)} = \vec{k}^{(1)} + \vec{k}^{(2)} \tag{S3}$$

$$\vec{k}^{(4)} = \vec{k}^{(2)} - \vec{k}^{(1)} \tag{S4}$$

$$\vec{k}^{(5)} = \vec{k}^{(3)} + \vec{k}^{(1)} = 2\vec{k}^{(1)} + \vec{k}^{(2)} \tag{S5}$$

$$\vec{k}^{(6)} = \vec{k}^{(4)} + \vec{k}^{(5)} = \vec{k}^{(1)} + 2\vec{k}^{(2)} \tag{S6}$$

$$\vec{k}^{(7)} = 2\vec{k}^{(1)} \tag{S7}$$

$$\vec{k}^{(8)} = 2\vec{k}^{(2)} \tag{S8}$$

$$\vec{k}^{(9)} = \vec{k}^{(7)} + \vec{k}^{(8)} = 2\vec{k}^{(1)} + 2\vec{k}^{(2)} \tag{S9}$$

The intensity of one phase image can be written as in equation (1) in the main text. The intensity spectrum of one phase image $\tilde{I}_m(k_x, k_y)$ is hence given by

$$\tilde{I}_m(k_x, k_y) = \tilde{I}^{(0)} + \frac{1}{2}\sum_{\substack{n=-9\\n\neq 0}}^{9} \underbrace{\left(\tilde{I}^{(n)}(\vec{k}) * \delta(\vec{k} - \vec{k}^{(n)})\right)}_{\tilde{I}^{(n)}(\vec{k}-\vec{k}^{(n)})} e^{-i\phi_{n0}} e^{-i\alpha_m^{(n)}} \quad . \tag{S10}$$

The factor ϕ_{n0} is the absolute phase of the n-th frequency in the first phase image. It only depends on the chosen coordinate system and can be neglected. $\delta(\vec{k} - \vec{k}^{(n)})$ is the Dirac delta distribution. For several phase images (several values of m), equation (S10) represents a linear system of equations .

Every recorded phase image contains totally 19 frequency shifted copies of the detected intensity spectrum $I^{(n)}(\vec{k} - \vec{k}^{(n)})$ ($n \in \{-9, \ldots, 9\}$), which correspond to 19 unknown magnitudes. Thus, the minimum number of phase images which have to be acquired is 19. The linear system of equations in (S10) may be rewritten in matrix notation:

$$\begin{pmatrix} I_1 \\ I_2 \\ I_3 \\ \vdots \\ I_M \end{pmatrix} = \hat{A} \cdot \begin{pmatrix} \tilde{I}^{(0)}(\vec{k}) \\ \frac{1}{2}\tilde{I}^{(1)}(\vec{k} - \vec{k}^{(1)}) \\ \frac{1}{2}\tilde{I}^{(-1)}(\vec{k} + \vec{k}^{(1)}) \\ \vdots \\ \frac{1}{2}\tilde{I}^{(-9)}(\vec{k} + \vec{k}^{(9)}) \end{pmatrix} \tag{S11}$$

M is a whole number greater or equal than 19. The matrix $\hat{A} := (a_{m,n})$ is given by $(a_{m,n}) = \exp(-i\alpha_m^{(n)})$. Inversion of $\hat{A}$ gives a

solution of (S11) (and (S10)).

The factor $\alpha_m^{(n)}$ is the relative phase of the n-th frequency in the m-th phase image relative to the first phase image. We assume a relative phase of

$$\alpha_2^{(n)} = \vec{k}^{(n)} \cdot \vec{\Delta}$$

of the second phase image, where $\vec{\Delta}$ is the relative spatial pattern shift from the first to the second image. If the spatial shift from one image to the next is $\vec{\Delta}$ for all phase images, $\alpha_m^{(n)}$ is given by

$$\alpha_m^{(n)} = (m-1)\vec{k}^{(n)} \cdot \vec{\Delta} \quad .$$

We can write

$$\alpha_m^{(1)} = (m-1)\vec{k}^{(1)} \cdot \vec{\Delta} \tag{S12}$$

$$\alpha_m^{(2)} = (m-1)\vec{k}^{(2)} \cdot \vec{\Delta} =: \kappa\alpha_m^{(1)} \quad . \tag{S13}$$

The parameter κ is defined as the ratio between the phase shift of the second frequency $\alpha_m^{(2)}$ and the first frequency $\alpha_m^{(1)}$. Inserting $\vec{k}^{(1)}$ and $\vec{k}^{(2)}$ from (S2) and $\vec{\Delta} = (\Delta_x, \Delta_y)^t$ into (S12) and (S13) gives a linear system of equations for Δ_x and Δ_y:

$$\begin{aligned}
\alpha_m^{(1)} &= (m-1)\frac{2\pi}{p}\Delta_y \\
\kappa\alpha_m^{(1)} &= (m-1)\frac{\pi}{p}[\sqrt{3}\Delta_x + \Delta_y]
\end{aligned}$$

Solving for Δ_x and Δ_y gives:

$$\Delta_x = \frac{p(2\kappa+1)}{2\pi\sqrt{3}}\alpha_2^{(1)} \tag{S14}$$

$$\Delta y = \frac{p}{2\pi}\alpha_2^{(1)} \tag{S15}$$

$$\Rightarrow |\vec{\Delta}| = \frac{p}{\sqrt{3}\pi}\sqrt{\kappa^2+\kappa+1} \tag{S16}$$

From (S14) and (S15) it follows that only the y component of the shift vector depends on the parameter κ and the direction of the shift vector to be given by:

$$\tan(\theta) = \left(\frac{\sqrt{3}}{(2\kappa+1)}\right) \tag{S17}$$

If the absolute value of the shift vector $\Delta := |\vec{\Delta}|$ is chosen to be

$$\Delta = \frac{p}{19\cos(\angle(\vec{k}^{(1)}, \vec{\Delta}))} \quad ,$$

the relative phase shifts are given by

$$\alpha_m^{(0)} = 0 \ , \qquad \alpha_m^{(1)} = (m-1)\frac{2\pi}{19} \ , \qquad \alpha_m^{(2)} = (m-1)\kappa\frac{2\pi}{19} \quad .$$

From the relations (S3) - (S9) it follows that the remaining relative phase shifts are given by:

$$\begin{aligned}
\alpha_m^{(3)} &= (m-1)(1+\kappa)\frac{2\pi}{19} \\
\alpha_m^{(4)} &= (m-1)(\kappa-1)\frac{2\pi}{19} \\
\alpha_m^{(5)} &= (m-1)(2+\kappa)\frac{2\pi}{19} \\
\alpha_m^{(6)} &= (m-1)(1+2\kappa)\frac{2\pi}{19} \\
\alpha_m^{(7)} &= (m-1)(2)\frac{2\pi}{19} \\
\alpha_m^{(8)} &= (m-1)(2\kappa)\frac{2\pi}{19} \\
\alpha_m^{(9)} &= (m-1)(2+2\kappa)\frac{2\pi}{19} \\
\alpha_m^{(-n)} &= -\alpha_m^{(n)}
\end{aligned}$$

Thus, the entries of the matrix $\hat{A}$ are functions of the parameter κ and hence a function of the shift angle θ in (S17).
In order to get a solvable linear system of equations, the determinant of $\hat{A}$ may not vanish ($\det \hat{A} \neq 0$). This condition limits the choice of κ. Furthermore one gets the best error propagation of the solution of (S11), if the matrix $\hat{A} = (a_{m,n}) = \exp(-i\alpha_m^{(n)})$ is proportional to a unitary matrix. $\hat{A}$ becomes unitary, if all values $\alpha_m^{(n)}$ are whole numbered multiples of $2\pi/19$ and pairwise different. This is the case, if κ is chosen to be

$$\kappa_1 = 7 \tag{S18}$$

or

$$\kappa_2 = 11 \quad . \tag{S19}$$

In order to minimize the total shift displacement Δ (equation (S16)), it is favorable to choose $\kappa = \kappa_1 = 7$. Inserting κ_1 into (S17), gives the orientation angle for the shift vector $\theta_1 \approx 6.59°$. The corresponding shift vector Δ is drawn in figure S3c) and S3e). The second shift direction which allows a unitary solution of the unknown frequency bands contributions is $\theta_2 \approx 4.31°$.

Supplementary Note 2: Necessary excitation line width

In order to generate a patterned excitation intensity in the sample, we illuminate a SIM phase substrate with a laser line and image it onto the microscopic sample. That means the pattern contrast for one phase image is generated sequentially by moving the laser line across the SIM substrate. For one point in time, an excitation line as shown in figure 2b) is generated. The pattern contrast of this excitation line arises only by interference of the hexagonal diffraction orders. Thus, the line has to have a minimum width in the y-direction, in order to allow excitation waves to interfere and get a homogeneous distribution of contrasts for all hexagon (intensity) frequencies.

The integral of the line excitation over all line positions gives an integrated patterned excitation intensity. The laser line has been assumed to have a Gaussian profile in y-direction

$$I_{\mathrm{LASER}}(y) = I_{\max} \exp\left(-\frac{1}{2}\left(\frac{y - y_l}{\sigma}\right)^2\right) \quad .$$

$I_{\max}$ is the maximum intensity in the center of the excitation line, which is located at y_l and σ is the root mean square (RMS) of the Gaussian distribution and is clearly connected with the full width at half maximum (FWHM) of the line. The integrated excitation contrasts for $\vec{k}^{(1)}$, $\vec{k}^{(2)}$ and $\vec{k}^{(3)}$ are shown in figure S4a) as a function of σ, which is scaled in units of hexagon periods. Note, that the contrast of $\vec{k}^{(2)}$ coincides with the contrast of $\vec{k}^{(3)}$ because of symmetry. The same plot for the contrasts of $\vec{k}^{(4)}$, $\vec{k}^{(5)}$, $\vec{k}^{(6)}$ and $\vec{k}^{(7)}$, $\vec{k}^{(8)}$, $\vec{k}^{(9)}$ is shown in figure S4b) and (S4c) respectively. The contrasts for $\vec{k}^{(5)}$ and $\vec{k}^{(6)}$ coincide in figure S4b) and the contrasts of $\vec{k}^{(8)}$ and $\vec{k}^{(9)}$ coincide in figure S4c).

For a RMS value of $\sigma \approx 1.6p$, the excitation intensity contrasts give their theoretical values for all pattern intensity frequencies. This RMS corresponds approximately to a line width of 3 hexagon periods (FWHM).

The theoretical intensity contrasts are given by the ratio of all possible amplitude differences (compare to figure S3a) and the number of diffraction orders, if the interfering diffraction orders all have the same power. That means, the first order intensity frequencies $\vec{k}^{(1)}$, $\vec{k}^{(2)}$ and $\vec{k}^{(3)}$ have a theoretical contrast of $4/7 \approx 0.57$. The frequencies $\vec{k}^{(4)}$, $\vec{k}^{(5)}$, $\vec{k}^{(6)}$ have a contrast of $2/7 \approx 0.29$ and the second order frequencies $\vec{k}^{(7)}$, $\vec{k}^{(8)}$, $\vec{k}^{(9)}$ have a theoretical contrast value of $1/7 \approx 0.14$.

Supplementary Note 3: Influence of frequency verctors errors on resolution and homogeneity

Errors of the frequency vector can deteriorate resolution and homogeneity in SIM images/volumes. figure S7 demonstrates the influence of frequency errors: An artificial object of nanorulers (all oriented in y-direction) was assumed and a series of SIM phase images has been generated. We assumed, that the absolute values of the frequency vectors have no errors, but their angles have. figure S7 shows a SIM evaluation of the phase images without any errors of the frequency vectors. In figure S7b), an error of 0.5% (which corresponds to an angle error of 5mrad) was assumed. In figures S7c) and S7d), an error of 1% and 1.5% was assumed respectively. One can clearly see the loss in resolution and inhomogeneities over the field of view for erroneous frequency vectors.

Supplementary Note 4: Adjustment of shift angles and Calibration

A thin layer of fluorescent dye as used in [S4] has been used as microscopic object for the adjustment of shift angles and calibration.

The SIM phase pattern substrate was mounted on a rotatable disc (as shown in figure S1. A series of phase images $I_m(x, y)$ was recorded, while the phase shifting galvanometric scanner (see figure 1 and supplementary figure S1) shifted the pattern image between successive image acquisitions.

The calibration object does not exhibit spatial structures, thus only the zero frequency was contained in the object spatial frequency spectrum. Hence, the hexagonal frequency vectors can be found by peak detection, which can be refined e.g. by determination of the peak's center of gravity. Then, the phases

$$\phi_m^{(n)} := \arg\left(\sum_{x,y} I_m(x,y) \exp\left(-i[k_x^{(n)} x + k_y^{(n)} y]\right)\right) \tag{S20}$$

were evaluated at least for the base frequencies $\vec{k}^{(1)}$ and $\vec{k}^{(2)}$. The patterned excitation was shifted along the same displacement $\vec{\Delta}$ between succeeding image acquisitions. Thus the phases $\phi_m^{(n)} =: \phi^{(n)}(m)$ as functions of the image number m are sinusoidal functions. In order to determine the period of $\phi^{(n)}(m)$ for the base frequencies ($n = 1, 2$) in units of image numbers m, a model function

$$f^{(n)}(x) = a^{(n)} \sin(b^{(n)} m - c^{(n)}) \tag{S21}$$

was fitted to the data points by a nonlinear least square fit. The parameter κ is then given by

$$\kappa = \frac{b^{(2)}}{b^{(1)}}$$

If equation (S20) is evaluated for $\vec{k}^{(3)}$ also, a second calculation of κ can be carried out by evaluating

$$\kappa = \frac{b^{(3)}}{b^{(1)}} - 1 \quad .$$

This procedure is repeated for several orientations of the SIM phase pattern substrate until deviation of κ and its nominal value ($\kappa = 7$) is approximately below 0.1, which corresponds to a angle error

$$|\delta\theta| = \underbrace{\frac{\sqrt{3}}{2[1 + \kappa + \kappa^2]}}_{\approx 0.0162} \underbrace{\delta\kappa}_{\leq 0.1} \leq 1.62\text{mrad} = 0.09^\circ \quad ,$$

which is below 0.1°.

When the pattern orientation is been adjusted, the next step is to adjust the shift widths. A series of e.g. 38 images was recorded and equation (S20) is evaluated. Fitting the function (S21) to the values $\phi^{(1)}(m)$ gives the number of shifts ($2\pi/b^{(1)}$) which have to be applied to move the pattern across the whole length of the arrow indicated in figure S3e).
This procedure was repeated for several variations of the shift widths, until this shift number corresponded to the number of recorded images (38). If a different number of phase images is used, the shift widths are scaled linearly.

In order to calibrate the frequency vectors $\vec{k}^{(n)}$, the different information components $\tilde{I}^{(n)}(\vec{k}-\vec{k}^{(n)})$ have been compared in the regions of frequency space where they overlap [S1]. A sample with reasonable S/N can be used to record a series of phase images, which are Fourier transformed. By inversion of the matrix $\hat{A}$ in (S11), all frequency shifted versions of the image

$$\tilde{I}^{(n)}(\vec{k}-\vec{k}^{(n)}) = O_n(\vec{k})e^{i\Phi_{n0}}\tilde{S}(\vec{k}-\vec{k}^{(n)})$$

can be separated. The sample function is denoted by $\tilde{S}(\vec{k})$. The predetermined values for the frequency vectors $\vec{k}^{(n)}$ can be used to shift the frequency bands $\tilde{I}^{(n)}(\vec{k}-\vec{k}^{(n)})$ in Fourier space to their original (object) positions.

$$\tilde{I}^{(n)}(\vec{k}) = O_n(\vec{k}+\vec{k}^{(n)})e^{i\Phi_{n0}}\tilde{S}(\vec{k}) \quad .$$

Frequency shifts have been applied by multiplication with functions $e^{i\vec{k}^{(n)}\vec{x}}$ in real space. For any $n \neq 0$, $\tilde{I}^{(n)}(\vec{k})O_0(\vec{k})$ has been cross correlated with $\tilde{I}^{(0)}(\vec{k})O_n(\vec{k}+\vec{k}^{(n)})$.
The cross correlation was done in three steps: first a standard fast-Fourier-transform-based cross-correlation in frequency space (yielding values only at discrete frequency-space pixels), then parabolic interpolation to locate the peak of that cross-correlation to subpixel accuracy, and finally refinement through an optimization in which subpixel frequency-space shifts were applied in the form of real-space phase gradients. The location of the cross-correlation peak yields the frequency vector $\vec{k}^{(n)}$ [S1].

Supplementary Note 5: Hexagonal phase pattern design

The hexagonal phase pattern is a substrate, which modulates phases of a transmitting light wave by modulations of the optical path length through the substrate. The phase pattern used in this work is a binary phase pattern as shown in figure S5a). The path difference which is caused by the optical path difference ΔD is given by

$$\frac{2\pi}{\lambda}[n(D-\Delta D)+n_0\Delta D] = \underbrace{\frac{2\pi}{\lambda}nD}_{\Phi_0} - \underbrace{\frac{2\pi}{\lambda}(n-n_0)\Delta D}_{\Delta\Phi} \quad ,$$

where n is the refraction index of the glass substrate and n_0 is the diffraction index of the medium that surrounds the substrate (usually air, i.e. $n_0 = 1$). The optical path difference has been applied to a quartz glass substrate by dry etching in an hexagonal geometry as shown in figure S5b). The ratio of the gray areas in figure S5b) and the whole area is defined as the two-dimensional fill factor F_2 of the phase pattern. Equivalently, the fill factor can be calculated as the ratio of gray areas contained in an hexagonal unit cell (drawn dashed green) and the area of the unit cell. The gray area within the hexagonal unit cell is given by

$$\mathcal{A}_{\text{circ}} = 3R^2\pi = 3(F_1 p)^2\pi \quad .$$

F_1 is the one dimensional fill factor and defined as the ratio of the circle radius and the period of the hexagonal pattern. Note that the period of the hexagonal pattern is not given by the minimum distance of the circle centers but by the distance of two adjacent lines of circles figure (S5b)). The area of the hexagonal unit cell is given by

$$\mathcal{A}_{\text{hex}} = 6\frac{d}{2}\frac{d}{2}\sqrt{3} = \frac{3}{2}d^2\sqrt{3} = 2p^2\sqrt{3} \quad .$$

Thus, the two dimensional fill factor is given by

$$F_2 = \frac{\mathcal{A}_{\text{circ}}}{\mathcal{A}_{\text{hex}}} = \frac{\sqrt{3}}{2}F_1^2\pi \Leftrightarrow F_1 = \sqrt{\frac{2F_2}{\sqrt{3}\pi}} \quad .$$

If one assumes a phase difference of $\pi/2$ ($(n-n_0)\Delta D = \frac{\lambda}{2}$), the amplitude behind the phase pattern can be written as

$$\begin{aligned} U(\vec{x}_\perp) &= U_0\left[1 - 2F_2\sum_{n\neq 0}\text{jinc}(|\vec{k}^{(n)}|\ F_1 p)e^{i\vec{k}^{(n)}\vec{x}_\perp}\right] \\ &= U_0(1-2F_2) - 2U_0F_2\sum_{n\neq 0}\text{jinc}\,(2\pi F_1)\,e^{i\vec{k}^{(n)}\vec{x}_\perp} \quad . \end{aligned} \tag{S22}$$

The Fourier coefficients of the aplitude can be seen in equation (S22):

$$\begin{aligned} c_0 &= U_0(1-2F_2) \\ c_{\pm 1} &= -2U_0F_2\mathrm{jinc}\left(\sqrt{\frac{8F_2\pi}{\sqrt{3}}}\right) \end{aligned}$$

The absolute square of this coefficients correspond to the diffraction orders' intensities. Analogously to [S1], we designed the phase pattern such, that the zero diffraction order has approximately $70-80\%$ of the power of the first diffraction orders. This condition is met for two possible values of the two dimensional fill factor $F_2 \approx 0.62$ and $F_2 \approx 0.35$ as shown in figure S5c). In our experiments, we used a phase pattern substrate with a two dimensional fill factor of $F_2 \approx 0.62$.

Supplementary Note 6: Influence of polarization on pattern contrasts

When using a phase pattern in combination with coherent illumination, all patterned intensity contrast in the image (which corresponds to the microscopic object) arises due to interference of recombined pattern diffraction orders. If a linear polarization is used for the illumination, this leads to different pattern contrasts for different frequencies $\vec{k}^{(n)}$ of the hexagonal pattern. The combination of linear polarized diffraction orders can mathematically described by a generalized Jones formalism. The polarization angle relative to the x-axis is denoted by χ, and the diffraction angle for the first diffraction orders is denoted by α ($n\sin(\alpha) = \lambda/(p)$). The Fourier coefficients of the hexagonal excitation intensity are summarized in table 2 as functions of χ and α. All hexagonal diffraction orders are assumed to have the same intensity I_0.

n	$c_n(\alpha,\chi)/I_0$
0	7
1	$\frac{1}{8}[\cos^2(\chi)(23 + 12\cos(\alpha) - 3\cos(2\alpha)) + \sin^2(\chi)(3 + 28\cos(\alpha) + \cos(2\alpha))]$
2	$\frac{1}{4}\left[\begin{array}{l} 4\cos^2(\chi)(1 + 3\cos(\alpha)) + \sin^2(\chi)(9 + 8\cos(\alpha) - \cos(2\alpha))+ \\ \sin(\chi)\cos(\chi)(4\sqrt{3}(3 + \cos(\alpha))\sin^2(\frac{\alpha}{2})) \end{array}\right]$
3	$\frac{1}{4}\left[\begin{array}{l} 4\cos^2(\chi)(1 + 3\cos(\alpha)) + \sin^2(\chi)(9 + 8\cos(\alpha) - \cos(2\alpha))- \\ \sin(\chi)\cos(\chi)(4\sqrt{3}(3 + \cos(\alpha))\sin^2(\frac{\alpha}{2})) \end{array}\right]$
4	$\frac{1}{4}\left[\begin{array}{l} \cos^2(\chi)(2 + 6\cos(\alpha)) + \sin^2(\chi)(-1 + 6\cos(\alpha) + 3\cos(2\alpha)) + \\ \sin(\chi)\cos(\chi)6\sqrt{3}\sin^2(\alpha)) \end{array}\right]$
5	$\frac{1}{4}\left[\begin{array}{l} \cos^2(\chi)(2 + 6\cos(\alpha)) + \sin^2(\chi)(-1 + 6\cos(\alpha) + 3\cos(2\alpha)) - \\ \sin(\chi)\cos(\chi)6\sqrt{3}\sin^2(\alpha)) \end{array}\right]$
6	$\frac{1}{8}\left[\cos^2(\chi)(-5 + 12\cos(\alpha) + 9\cos(2\alpha)) + \sin^2(\chi)(7 + 12\cos(\alpha) - 3\cos(2\alpha))\right]$
7	$\cos^2(\chi) + \sin^2(\chi)\cos(2\alpha)$
8	$\frac{1}{4}\left[\begin{array}{l} \cos^2(\chi)(1 + 3\cos(2\alpha)) + \sin^2(\chi)(3 + \cos(2\alpha)) + \\ \sin(\chi)\cos(\chi)4\sqrt{3}\sin^2(\alpha)) \end{array}\right]$
9	$\frac{1}{4}\left[\begin{array}{l} \cos^2(\chi)(1 + 3\cos(2\alpha)) + \sin^2(\chi)(3 + \cos(2\alpha)) - \\ \sin(\chi)\cos(\chi)4\sqrt{3}\sin^2(\alpha)) \end{array}\right]$

Table 2: The Fourier coefficients of the hexagonal excitation intensity with linear polarization as functions of the polarization angle χ and the diffraction angle α.

The coefficients from table 2 are plotted for an assumed diffraction angle $\alpha \approx 67.3°$ in figures S6a) -c).

When using linear polarization, a compromise concerning the excitation contrasts has to be found. While the frequency bands

$\vec{k}^{(1)}$ - $\vec{k}^{(3)}$ are responsible for confocality and axial resolution enhancement, the frequency bands $\vec{k}^{(7)}$ - $\vec{k}^{(9)}$ are required for lateral resolution enhancement. the frequency bands corresponding to $\vec{k}^{(4)}$ - $\vec{k}^{(6)}$ are in principle not required.

A polarization parallel to the excitation line $\chi = 0°$ gives best contrast values for modulations orthogonal to the excitation linie (c_1, c_7), but quite low contrasts for c_8 and c_9. A polarization parallel to the excitation line ($\chi = 90°$) leads to a normed contrast of 0.57 for $\vec{k}^{(8)}$ and $\vec{k}^{(9)}$ and 0.70 for $\vec{k}^{(7)}$. This corresponds to a standard deviation of 0.0751 or 12.2% for the contrasts of $\vec{k}^{(7)}$, $\vec{k}^{(8)}$ and $\vec{k}^{(9)}$. The deviation for the freqeuncies $\vec{k}^{(1)}$, $\vec{k}^{(2)}$ and $\vec{k}^{(3)}$ amounts 0.2240 or 33.5% for $\chi = 90°$. Because the normed contrast of $\vec{k}^{(1)}$ is only half of the contrasts of $\vec{k}^{(2)}$ and $\vec{k}^{(3)}$, confocality is reduced in the direction of $\vec{k}^{(1)}$ (the y-direction). This is compensated by the confocality of the line scanner in y-direction.
Thus, we chose a linear polarization angle of $\chi = 90°$ in our measurements, i.e. the polarization was set orthogonal to the excitation line.

As illustrated in figure S3), the base frequencies of the hexagonal excitation intensities can be split into a z-dependent contribution and one that does not depend on defocus z. Analogously, the excitation Fourier coefficients from table 2 can be split into corresponding contributions, which are summarized in table 3.

n	$c_n^{(z)}(\alpha,\chi)/I_0$	$c_n^{(0)}(\alpha,\chi)/I_0$
1	$2\cos^2(\chi) + 2\cos(\alpha)\sin^2(\chi)$	$\frac{1}{8}\left[\begin{array}{l}\cos^2(\chi)(7 + 12\cos(\alpha) - 3\cos(2\alpha))+\\ +\sin^2(\chi)(3 + 12\cos(\alpha) + \cos(2\alpha))\end{array}\right]$
2	$\cos^2(\chi)\left[\frac{1}{2} + \frac{3}{2}\cos(\alpha)\right]+$ $+\sin^2(\chi)\left[\frac{3}{2} + \frac{1}{2}\cos(\alpha)\right]+$ $+\sin(\chi)\cos(\chi)\left[\sqrt{3}(1-\cos(\alpha))\right]$	$\cos^2(\chi)\left[\frac{1}{2} + \frac{3}{2}\cos(\alpha)\right]+$ $+\sin^2(\chi)\left[\frac{3}{4} + \frac{3}{2}\cos(\alpha) - \frac{1}{4}\cos(2\alpha)\right]+$ $+\sin(\chi)\cos(\chi)\left[\frac{1}{2}\sqrt{3}\sin^2(\alpha)\right]$
3	$\cos^2(\chi)\left[\frac{1}{2} + \frac{3}{2}\cos(\alpha)\right]+$ $+\sin^2(\chi)\left[\frac{3}{2} + \frac{1}{2}\cos(\alpha)\right]$ $-\sin(\chi)\cos(\chi)\left[\sqrt{3}(1-\cos(\alpha))\right]$	$\cos^2(\chi)\left[\frac{1}{2} + \frac{3}{2}\cos(\alpha)\right]+$ $+\sin^2(\chi)\left[\frac{3}{4} + \frac{3}{2}\cos(\alpha) - \frac{1}{4}\cos(2\alpha)\right]$ $-\sin(\chi)\cos(\chi)\left[\frac{1}{2}\sqrt{3}\sin^2(\alpha)\right]$

Table 3: The decomposition of the coefficients $c_n(\chi)|n \in \{1,2,3\}$ in a z-dependent and an z-independent contribution. The following equation is valid: $c_n(\chi) = c_n^{(z)}(\chi) + c_n^{(0)}(\chi)\forall n \in \{1,2,3\}$. The coefficients in this table are plotted in figures S6 d) - f) for a diffraction angle $\alpha \approx 67.3°$ as functions of χ.

This coefficients are illustrated in figures S6 d) - f) for a diffraction angle $\alpha \approx 67.3°$. The deviation of the two contributions is small for all polarization directions χ.

Supplementary References

[S1] Gustafsson, M. G. L., et al. Three-Dimensional Resolution Doubling in Wide-Field Fluorescence Microscopy by Structured Illumination. *Biophysical Journal* **94**(June), 4957–4970 (2008).

[S2] Neil, M. A., Juskaitis, R., & Wilson, T. Method of obtaining optical sectioning by using structured light in a conventional microscope. *Optics letters* **22**(24), 1905–7 (1997).

[S3] Schropp, M. & Uhl, R. Two-dimensional structured illumination microscopy. *Journal of Microscopy* **256**(1), 23–36 (2014).

[S4] Brakenhoff, G. J., et al. Characterization of sectioning fluorescence microscopy with thin uniform fluorescent layers: Sectioned Imaging Property or SIPcharts. *Journal of microscopy* **219**(3), 122–32 (2004).